Isogeometric vibration of the magneto-electro-elastic sandwich plate with functionally graded carbon nanotube reinforced composite core

P.T. HUNG[1,*], *T. NGUYEN-Thanh*[2], *P. PHUNG-Van*[2], *H. NGUYEN-Gia*[2]

[1]Faculty of Civil Engineering, Ho Chi Minh City University of Technology and Education, Ho Chi Minh City, Vietnam
[2]Faculty of Civil Engineering, HUTECH University, Ho Chi Minh City, Vietnam

*Corresponding Author: P.T. Hung (Email: hungpht@hcmute.edu.vn)
(Received: 01-August-2023; accepted: 07-Sep-2023; published: 30-Sep-2023)
http://dx.doi.org/10.55579/jaec.202373.428

Abstract. *This paper investigates the free vibration analysis of the magneto-electro-elastic (MEE) sandwich plates with functionally graded carbon nanotube reinforced composite (FG-CNTRC) core using isogeometric approach (IGA). The sandwich plate is composed of the homogeneous MEE face sheets and FG-CNTRC core with four types of carbon nanotubes (CNTs) distribution, including CNT-UD, CNT-O, CNT-V and CNT-X. The external electric voltage and magnetic potential are applied in the top and bottom layers of the MEE sandwich plate. Employing the refined plate theory (RPT) and Hamilton principle, the governing equation for free vibration of the MEE sandwich plate is derived. The IGA employs Non-Uniform Rational B-Splines (NURBS) basic functions to approximate the displacement fields and the magnetic and electric potentials in the RPT model. The study examines and discusses the impact of different factors on the frequency of the MEE sandwich plate, including parameters like CNTs distributions, CNTs volume fraction, external electric voltage and magnetic potential, and the geometrical parameter of the plate. This research has revealed several important discoveries regarding the fabrication of MEE sandwich structures.*

Keywords

Magneto-electro-elastic sandwich plate, functionally graded carbon nanotube reinforced composite, isogeometric analysis, free vibration, refined plate theory

1. Introduction

Magneto-electro-elastic materials are composite materials that possess the ability to respond to mechanical, electrical, and magnetic stimuli. The unique properties of these materials stem from their ability to undergo mechanical deformation under applied stress, generate electric charges when subjected to mechanical forces, and exhibit changes in their magnetic properties in response to magnetic fields. MEE structures can actively control vibrations, harvest energy, and act as sensors, making them versatile and promising for various industries and fields of research. Consequently, there has been a surge in research to understand the mechanical characteristics of MEE structures in recent years. Pan and Han [1] found an exact solution of the multilayered plate made of anisotropic

and functionally graded (FG) MEE materials. Based on the Kirchhoff thin-plate theory (KPT) and analytical method, the static bending of the MEE thin plate was presented by Liu [2]. The free vibration of the laminated plate composed of the homogeneous piezoelectric and piezomagnetic layers was introduced by Ramirez *et al.* [3] according to the Ritz method. Li *et al.* [4] found the analytical natural frequency of the MEE plate resting on an elastic foundation using the Mindlin theory. In addition, Ansari *et al.* [5] employed the combination of nonlinear first-order plate theory and nonlocal elasticity theory to express the buckling and post-buckling behavior of the magneto-electro-thermo-elastic (METE) nanoplates. The nonlocal strain gradient theory (NSGT) and the FSDT were used by Malikan and coworkers [6] to study the analytical forced vibration of the MEE nanoplates. Via the nonlocal elastic theory and the third-order beam theory, the thermal buckling of the METE FG nanobeams was studied by Ebrahimi *et al.* [7] using the analytical method. Conversely, Xin and Hu [8] used the semi-analytical method to investigate the vibration of the multilayer MEE rectangular plates under the simply supported boundaries. With the help of Reddy's higher-order shear deformation plate theory (HSDT), the critical buckling load of the MEE plates was found by Razavi [9] based on the analytical method. The vibration analysis of the MEE plates on an elastic foundation was presented by Shooshtari and Razavi [10] according to the HSDT and analytical method. The analytical static bending and vibration responses of the MEE circular plate, considering the surface effect, were carried out by Yang *et al.* [11] via the KPT. Solby and Mukahal [12] used the RPT and analytical method to present the free vibration of the FG MEE plate reinforced by graphene platelets and resting on an elastic foundation. Besides, Arefi *et al.* [13] investigated the analytical buckling and static bending of the multilayered doubly curved nanoshell with the MEE face sheets and homogeneous core employing the nonlocal elasticity theory. Mohammadrezazadeh [14] found the linear and nonlinear natural frequencies of the MEE composite conical shells resting on a nonlinear elastic foundation based on the analytical method. FG-CNTRC materials posed applications in aerospace, energy, automobile, medicine, structural...due to their mechanical, thermal and electrical outstanding properties. Therefore, many researchers have paid attention to these materials. Based on the higher-order shear deformation theory (HSDT), the analytical nonlinear bending and large amplitude vibration of FG-CNTRC plates in thermal environment were studied by Shen [15] and Wang [16]. A combination of the FSDT and kp-Ritz method was used by Lei *et al.* [17] to calculate the frequency of the laminated rectangular plates with the FG-CNTRC layers. Also, Zhang *et al.* [18] found the analytical solution of the free vibration of the skew plates made of FG-CNTRC materials based on the FSDT. According to the FSDT, Pouresmaeeli *et al.* [19] employed Galerkin's method to present the vibration of double-curved FG-CNTRC shell panels. Next, the vibration analysis of the arbitrarily shape cutout FG-CNTRC plate was researched by Ansari *et al.* [20] utilizing the variational differential quadrature finite element method. According to the third-order shear deformation plate theory (TSDT) and Galerkin's method, the vibration and dynamic response of the sandwich plates with FG-CNTRC top and bottom layers are presented by Dat *et al.* [21]. Cheshmeh *et al.* [22] used HSDT with 12 variables to find the analytical natural frequency and critical buckling load of the FG-CNTRC plates in thermal environment. Due to its reliance on Non-uniform rational B-splines basic functions, the IGA can effectively handle higher-order derivatives of the refined plate theory. These NURBS basic functions offer versatility in achieving the desired level of continuity within the basis functions. Hughes [23] was the first to propose the IGA along with its computational expense. According to IGA, Bazilevs et al. [24] conducted an analysis of wind turbines and turbomachinery, while Takizawa *et al.* [25] analyzed computational cardiovascular medicine. Zhang et al. [26] examined advancements in the nonlocal operator method, an innovative approach for solving PDEs and addressing complex engineering challenges. Besides, references [27–29] demonstrate that IGA allows for investigating microplate size-dependent free vibration, bending, and buckling. Considering

the mentioned references, no prior investigation utilizing the IGA and RPT has been conducted to study the behaviors of the MEE sandwich plate with the FG-CNTRC core. This article addresses the research gap by employing RPT and IGA to analyze the free vibration of the MEE sandwich plates with the FG-CNTRC core. The influence of the CNTs distribution, CNTs volume fraction, external electric and magnetic loads and geometries on the natural frequency of the MEE sandwich plate with FG-CNTRC core is examined and discussed in detail. The novel findings offer valuable insights into the free vibration behaviors of MEE-FGP plates, potentially contributing to the design and optimization of these structures for improved practical performance.

2. The basic equations

2.1. The material properties

Let us consider the sandwich rectangular plate with length a, width b and thickness h, as shown in Figure 1. The MEE face sheets of the MEE sandwich plate comprise piezoelectric (BaTiO3) and piezomagnetic (CoFe2O4) materials. In this investigation, the volume fractions of BaTiO3 and CoFe2O4 are taken by 0.5. The material properties of the MEE face sheets are shown in Table 1.

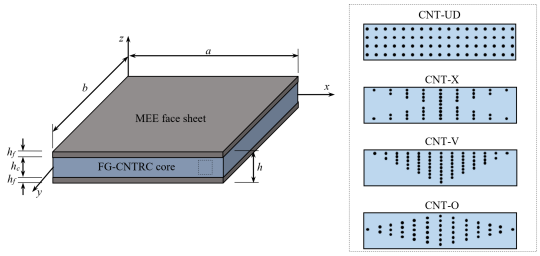

Fig. 1: The geometry of the MEE sandwich plate with the FG-CNTRC core.

Besides, the FG-CNTRC core is made of the matrix epoxy reinforced by the CNTs with four CNTs distributions: CNT-UD, CNT-O, CNT-V and CNT-X. By using the extended rule of mixture [31], the effective material properties of the

Tab. 1: The material properties of the MEE material [30].

Properties	BaTi2O3-CoFe2O4
Elastic (GPa)	$c_{11} = c_{22} = 226$; $c_{12} = 125; c_{13} = 124$; $c_{33} = 216; c_{66} = 50.5$; $c_{44} = c_{55} = 44.2$
Piezoelectric (Cm^{-2})	$e_{31} = e_{32} = -2.2$; $e_{33} = 9.3$; $e_{15} = 5.8$
Piezomagnetic (N/Am)	$q_{15} = q_{24} = 275$; $q_{31} = q_{32} = 290.1$ $q_{33} = 349.9$
Dielectric (10^{-9} $C^2m^{-2}N^{-1}$)	$k_{11} = k_{22} = 5.64$; $k_{33} = 6.35$
Magnetic ($10^{-6}Ns^2/C^2$)	$\mu_{11} = \mu_{22} = -297$; $\mu_{33} = 83.5$
Magnetoelectric (10^{-12} Ns/VC)	$d_{11} = d_{22} = 5.367$; $d_{33} = 2737.5$
Density (kg/m^3)	$\rho^f = 5550$

FG-CNTRC core layer are presented as follows

$$\begin{cases} E_{11}^c = \eta_1 V_{CNT} E_{11}^{CNT} + V_m E^m; \\ E_{22}^c = \frac{\eta_2}{V_{CNT}/E_{22}^{CNT} + V_m/E^m}; \\ G_{12}^c = \frac{\eta_3}{V_{CNT}/G_{12}^{CNT} + V_m/G^m}; \\ \nu_{12}^c = V_{CNT}\nu_{12}^{CNT} + V_m\nu_m; \\ \rho^c = V_{CNT}\rho_{CNT} + V_m\rho_m \end{cases} \quad (1)$$

where symbol "c" indicates the core layer; E_{11}^{CNT} and E_{22}^{CNT} represent the Young modulus of the CNTs; G_{12}^{CNT} is the shear modulus of the CNTs; E^m and G^m denote Young's and shear modulus of the matrix, respectively; v_m and v_{12}^{CNT} are Poisson's ratios of the matrix and CNTs, respectively; ρ_{CNT} and ρ_m represent the mass density of CNTs and matrix, respectively; η_1, η_2 and η_3 are the CNTs efficiency parameters; V_{CNT} and V_m are the volume fractions of the CNTs and matrix, respectively. The material properties of the matrix and CNTs are given in Table 2 [32].

Furthermore, the relationship between and is presented as follow

$$V_{CNT} + V_m = 1 \quad (2)$$

In this article, four distribution patterns are employed to reinforce CNTs within the material matrix throughout the thickness of the plate. The CNTs volume fraction V_{CNT} in Eqs. 1 and

Tab. 2: The material properties of the matrix and CNTs.

Properties	Matrix	CNTs
Elastic (GPa)	$E_m = 2.5$	$E_{11}^{CNT} = 5645.1$ $E_{22}^{CNT} = 7080$ $G_{12}^{CNT} = 1946.6$
Poisson'sratio ratio	$\nu_m = 0.34$	$\nu_{12}^{CNT} = 0.175$
Density (kg/m^3)	$\rho_m = 1160$	$\rho_{CNT} = 1400$

2, for various CNTs distributions, is described as follows

$$\begin{cases} V_{CNT} = \hat{V}_{CNT} & \text{CNT} - \text{UD}; \\ V_{CNT}(z) = \left(2 - \frac{4|z|}{h_c}\right)\hat{V}_{CNT} & \text{CNT} - \text{O}; \\ V_{CNT}(z) = \left(1 + \frac{2z}{h_c}\right)\hat{V}_{CNT} & \text{CNT} - \text{V}; \\ V_{CNT}(z) = \frac{4|z|}{h_c}\hat{V}_{CNT} & \text{CNT} - X \end{cases} \tag{3}$$

where

$$\hat{V}_{CNT} = \frac{w_{CNT}}{w_{CNT} + \frac{\rho_{CNT}}{\rho_m}(1 - w_{CNT})} \tag{4}$$

in which w_{CNT} denotes the mass fraction of CNTs. Besides, the CNTs efficiency parameters are defined as follows [33]

$$\begin{cases} \eta_1 = 0.137, \eta_2 = 1.022, \eta_3 = 0.715 \text{ for } \hat{V}_{CNT} = 0.12; \\ \eta_1 = 0.142, \eta_2 = 1.626, \eta_3 = 1.138 \text{ for } \hat{V}_{CNT} = 0.17; \\ \eta_1 = 0.141, \eta_2 = 1.585, \eta_3 = 1.109 \text{ for } \hat{V}_{CNT} = 0.28 \end{cases} \tag{5}$$

2.2. The refined plate theory

Employing the RPT [34], the displacement vector u of the MEE sandwich plate is presented as follows

$$\mathbf{u} = \begin{Bmatrix} u \\ v \\ w \end{Bmatrix} = \mathbf{u}_1 + z\mathbf{u}_2 + f(z)\,\mathbf{u}_3 = \begin{Bmatrix} u_0 \\ v_0 \\ w_b + w_s \end{Bmatrix} + z\begin{Bmatrix} -w_{b,x} \\ -w_{b,y} \\ 0 \end{Bmatrix} + f(z)\begin{Bmatrix} w_{s,x} \\ w_{s,y} \\ 0 \end{Bmatrix} \tag{6}$$

in which u_0 and v_0 denote the in-plane displacement of the middle plane, whereas w_b and w_s are the transverse displacements in terms of their bending and shear components, respectively; symbol "," stands for the differential operator; $f(z) = -\frac{4z^3}{3h^2}$ denotes the distribution function. According to [35], the RPT with four variables is free from the shear locking without the shear correction factor. This is because of the second-order distribution of the shear stress through the plate thickness.

According to the displacement vector in Eq. (6), the linear strain tensor is formulated by

$$\boldsymbol{\varepsilon} = \begin{Bmatrix} \boldsymbol{\varepsilon}_b \\ \boldsymbol{\varepsilon}_s \end{Bmatrix} = \begin{Bmatrix} \boldsymbol{\varepsilon}_{b1} + z\boldsymbol{\varepsilon}_{b2} + f(z)\boldsymbol{\varepsilon}_{b3} \\ (1 + f'(z))\boldsymbol{\gamma}_s \end{Bmatrix} \tag{7}$$

in which symbol "′" represents the derivative with respect to z, and

$$\boldsymbol{\varepsilon}_b = \begin{Bmatrix} \varepsilon_x \\ \varepsilon_y \\ \gamma_{xy} \end{Bmatrix}; \boldsymbol{\varepsilon}_{b1} = \begin{Bmatrix} u_{0,x} \\ v_{0,y} \\ u_{0,y} + v_{0,x} \end{Bmatrix}; \boldsymbol{\varepsilon}_{b2} = -\begin{Bmatrix} w_{b,xx} \\ w_{b,yy} \\ 2w_{b,xy} \end{Bmatrix}; \varepsilon_{b3} = \begin{Bmatrix} w_{s,xx} \\ w_{s,yy} \\ 2w_{s,xy} \end{Bmatrix}; \boldsymbol{\varepsilon}_s = \begin{Bmatrix} \gamma_{xz} \\ \gamma_{yz} \end{Bmatrix}; \boldsymbol{\gamma}_s = \begin{Bmatrix} w_{s,x} \\ w_{s,y} \end{Bmatrix} \tag{8}$$

Based on Maxwell's equation, as elucidated in reference [36], the electric and magnetic potentials can be assumed as follows

$$\begin{cases} \Phi(x, y, z) = g(z)\varphi(x, y) + \frac{2z}{h}\varphi_0; \\ \Psi(x, y, z) = g(z)\psi(x, y) + \frac{2z}{h}\psi_0 \end{cases} \tag{9}$$

in which the electric potential, denoted as Φ, and the magnetic potential, represented as Ψ; the initial external electric voltage, referred to as φ_0, and the magnetic potential, indicated as ψ_0; $g(z) = -\cos(\pi z/h)$denotes the distributed function.

The magnetic and electric fields are obtained from the electric and magnetic potentials according to Eq. (9) as follows

$$\mathbf{E} = \begin{Bmatrix} E_x \\ E_y \\ E_z \end{Bmatrix} = \begin{Bmatrix} -\Phi_{,x} \\ -\Phi_{,y} \\ -\Phi_{,z} \end{Bmatrix} = \begin{Bmatrix} -g(z)\varphi_{,x} \\ -g(z)\varphi_{,y} \\ -g'(z)\varphi + \frac{2\varphi_0}{h} \end{Bmatrix}; \quad \mathbf{H} = \begin{Bmatrix} H_x \\ H_y \\ H_z \end{Bmatrix} = \begin{Bmatrix} -\Psi_{,x} \\ -\Psi_{,y} \\ -\Psi_{,z} \end{Bmatrix} = \begin{Bmatrix} -g(z)\psi_{,x} \\ -g(z)\psi_{,y} \\ -g'(z)\psi + \frac{2\psi_0}{h} \end{Bmatrix} \tag{10}$$

where the components of the electric field, namely E_x, E_y, and E_z, and the components of the magnetic field, namely H_x, H_y, and H_z.

2.3. Constitutive equations

For the MEE face sheets, the constitutive relations considering the coupling between elas-

tic, electric, and magnetic are expressed as follows [37,38]

$$\begin{Bmatrix} \sigma_x^f \\ \sigma_y^f \\ \tau_{xy}^f \\ \tau_{xz}^f \\ \tau_{yz}^f \end{Bmatrix} = \begin{bmatrix} \bar{c}_{11} & \bar{c}_{12} & 0 & 0 & 0 \\ \bar{c}_{12} & \bar{c}_{22} & 0 & 0 & 0 \\ 0 & 0 & \bar{c}_{66} & 0 & 0 \\ 0 & 0 & 0 & \bar{c}_{44} & 0 \\ 0 & 0 & 0 & 0 & \bar{c}_{55} \end{bmatrix} \begin{Bmatrix} \varepsilon_x \\ \varepsilon_y \\ \gamma_{xy} \\ \gamma_{xz} \\ \gamma_{yz} \end{Bmatrix} - \begin{bmatrix} 0 & 0 & \bar{e}_{31} \\ 0 & 0 & \bar{e}_{31} \\ 0 & 0 & 0 \\ \bar{e}_{15} & 0 & 0 \\ 0 & \bar{e}_{15} & 0 \end{bmatrix} \begin{Bmatrix} E_x \\ E_y \\ E_z \end{Bmatrix} - \begin{bmatrix} 0 & 0 & \bar{q}_{31} \\ 0 & 0 & \bar{q}_{31} \\ 0 & 0 & 0 \\ \bar{q}_{15} & 0 & 0 \\ 0 & \bar{q}_{15} & 0 \end{bmatrix} \begin{Bmatrix} H_x \\ H_y \\ H_z \end{Bmatrix};$$

$$\begin{Bmatrix} D_x^f \\ D_y^f \\ D_z^f \end{Bmatrix} = \begin{Bmatrix} 0 & 0 & 0 & \bar{e}_{15} & 0 \\ 0 & 0 & 0 & 0 & \bar{e}_{15} \\ \bar{e}_{31} & \bar{e}_{31} & 0 & 0 & 0 \end{Bmatrix} \begin{Bmatrix} \varepsilon_x \\ \varepsilon_y \\ \gamma_{xy} \\ \gamma_{xz} \\ \gamma_{yz} \end{Bmatrix} + \begin{bmatrix} \bar{k}_{11} & 0 & 0 \\ 0 & \bar{k}_{22} & 0 \\ 0 & 0 & \bar{k}_{33} \end{bmatrix} \begin{Bmatrix} E_x \\ E_y \\ E_z \end{Bmatrix} + \begin{bmatrix} \bar{d}_{11} & 0 & 0 \\ 0 & \bar{d}_{22} & 0 \\ 0 & 0 & \bar{d}_{33} \end{bmatrix} \begin{Bmatrix} H_x \\ H_y \\ H_z \end{Bmatrix};$$

$$\begin{Bmatrix} B_x^f \\ B_y^f \\ B_z^f \end{Bmatrix} = \begin{Bmatrix} 0 & 0 & 0 & \bar{q}_{15} & 0 \\ 0 & 0 & 0 & 0 & \bar{q}_{15} \\ \bar{q}_{31} & \bar{q}_{31} & 0 & 0 & 0 \end{Bmatrix} \begin{Bmatrix} \varepsilon_x \\ \varepsilon_y \\ \gamma_{xy} \\ \gamma_{xz} \\ \gamma_{yz} \end{Bmatrix} + \begin{bmatrix} \bar{d}_{11} & 0 & 0 \\ 0 & \bar{d}_{22} & 0 \\ 0 & 0 & \bar{d}_{33} \end{bmatrix} \begin{Bmatrix} E_x \\ E_y \\ E_z \end{Bmatrix} + \begin{bmatrix} \bar{\mu}_{11} & 0 & 0 \\ 0 & \bar{\mu}_{22} & 0 \\ 0 & 0 & \bar{\mu}_{33} \end{bmatrix} \begin{Bmatrix} H_x \\ H_y \\ H_z \end{Bmatrix} \tag{11}$$

where σ_x^f, σ_y^f, σ_{xy}^f, σ_{xz}^f and σ_{yz}^f are the stress components and electric displacements, respectively; B_x^f, B_y^f and B_z^f are the magnetic displacements; $\bar{c}_{ij}$ represents the reduced elastic coefficient; $\bar{e}_{ij}$ is the reduced piezoelectric coefficients; $\bar{q}_{ij}$ is the reduced piezomagnetic coefficient; $\bar{k}_{ij}$ is the reduced dielectric permittivity; is the reduced electromagnetic permittivity coefficient; is the reduced magnetic permittivity coefficient. In Eq. (11), the reduced coefficients are presented as follows

$$\begin{aligned} &\bar{c}_{11} = c_{11} - \frac{c_{13}^2}{c_{33}};\ \bar{c}_{12} = c_{12} - \frac{c_{13}^2}{c_{33}}; \\ &\bar{c}_{66} = c_{66};\ \bar{c}_{55} = c_{55};\ \bar{c}_{44} = c_{44}; \\ &\bar{e}_{31} = e_{31} - \frac{e_{33}c_{13}}{c_{33}};\ \bar{e}_{15} = e_{15}; \\ &\bar{q}_{31} = q_{31} - \frac{q_{33}c_{13}}{c_{33}};\ \bar{q}_{15} = q_{15}; \\ &\bar{k}_{33} = k_{33} + \frac{e_{33}^2}{c_{33}};\ \bar{k}_{11} = k_{11}; \\ &\bar{d}_{33} = d_{33} + \frac{q_{33}e_{33}}{c_{33}};\ \bar{d}_{11} = d_{11}; \\ &\bar{\mu}_{33} = \mu_{33} + \frac{q_{33}^2}{c_{33}};\ \bar{\mu}_{11} = \mu_{11} \end{aligned} \tag{12}$$

in which the coefficients c_{ij}, e_{ij}, q_{ij}, k_{ij}, d_{ij} and μ_{ij} are taken from Table 1 . The constitutive equations Eq. (11) in matrix form are reformulated as follows

$$\begin{cases} \boldsymbol{\sigma}_b^f = \mathbf{C}_{uub}^f \boldsymbol{\varepsilon}_b - \mathbf{C}_{ueb}\mathbf{E}_b - C_{umb}\mathrm{H}_b; \\ \boldsymbol{\sigma}_s^f = \mathbf{C}_{uus}^f \boldsymbol{\varepsilon}_s - \mathbf{C}_{ues}\mathbf{E}_s - \mathbf{C}_{um}\mathrm{H}_s; \\ \mathbf{D}_b^f = \mathbf{C}_{ueb}^T \boldsymbol{\varepsilon}_b + \mathbf{C}_{eeb}\mathbf{E}_b + \mathbf{C}_{emb}\mathrm{H}_b; \\ \mathbf{D}_s^f = \mathbf{C}_{ues}^T \boldsymbol{\varepsilon}_s + \mathbf{C}_{ees}\mathbf{E}_s + \mathbf{C}_{ems}\mathrm{H}_s; \\ \mathbf{B}_b^f = \mathbf{C}_{umb}^T \boldsymbol{\varepsilon}_b + \mathbf{C}_{emb}\mathbf{E}_b + \mathbf{C}_{mmb}\mathrm{H}_b; \\ \mathbf{B}_s^f = \mathbf{C}_{ums}^T \boldsymbol{\varepsilon}_s + \mathbf{C}_{ems}\mathbf{E}_s + \mathbf{C}_{mms}\mathrm{H}_s \end{cases} \tag{13}$$

in which

$$\begin{aligned} &\boldsymbol{\sigma}_b^f = \begin{Bmatrix} \sigma_x & \sigma_y & \tau_{xy} \end{Bmatrix}^T;\ \mathbf{D}_b^f = \begin{Bmatrix} 0 & 0 & D_z^f \end{Bmatrix}^T; \\ &\mathbf{B}_b^f = \begin{Bmatrix} 0 & 0 & B_z^f \end{Bmatrix}^T;\ \mathbf{E}_b = \begin{Bmatrix} 0 & 0 & E_z \end{Bmatrix}^T; \\ &\boldsymbol{\sigma}_s^f = \begin{Bmatrix} \tau_{xz} & \tau_{yz} \end{Bmatrix}^T;\ \mathbf{D}_s^f = \begin{Bmatrix} D_x^f & D_y^f \end{Bmatrix}^T; \\ &\mathbf{B}_s^f = \begin{Bmatrix} B_x^f & B_y^f \end{Bmatrix}^T;\ \mathbf{E}_s = \begin{Bmatrix} E_x & E_y \end{Bmatrix}^T; \\ &\mathbf{H}_b = \begin{Bmatrix} 0 & 0 & H_z \end{Bmatrix}^T;\ \mathbf{H}_s = \begin{Bmatrix} H_x & H_y \end{Bmatrix}^T \end{aligned} \tag{14}$$

and

$$\begin{aligned} &\mathbf{C}_{uub}^f = \begin{bmatrix} \bar{c}_{11} & \bar{c}_{12} & 0 \\ \bar{c}_{12} & \bar{c}_{22} & 0 \\ 0 & 0 & \bar{c}_{66} \end{bmatrix};\ \mathbf{C}_{uus}^f = \begin{bmatrix} \bar{c}_{44} & 0 \\ 0 & \bar{c}_{55} \end{bmatrix}; \\ &\mathbf{C}_{ueb} = \begin{bmatrix} 0 & 0 & \bar{e}_{31} \\ 0 & 0 & \bar{e}_{31} \\ 0 & 0 & 0 \end{bmatrix};\ \mathbf{C}_{ues} = \begin{bmatrix} \bar{e}_{15} & 0 \\ 0 & \bar{e}_{15} \end{bmatrix}; \\ &C_{umb} = \begin{bmatrix} 0 & 0 & \bar{q}_{31} \\ 0 & 0 & \bar{q}_{31} \\ 0 & 0 & 0 \end{bmatrix};\ C_{ums} = \begin{bmatrix} \bar{q}_{15} & 0 \\ 0 & \bar{q}_{15} \end{bmatrix}; \\ &\mathbf{C}_{eeb} = \begin{bmatrix} 0 & 0 & 0 \\ 0 & 0 & 0 \\ 0 & 0 & \bar{k}_{33} \end{bmatrix};\ \mathbf{C}_{ees} = \begin{bmatrix} \bar{k}_{11} & 0 \\ 0 & \bar{k}_{11} \end{bmatrix}; \\ &C_{mmb} = \begin{bmatrix} 0 & 0 & 0 \\ 0 & 0 & 0 \\ 0 & 0 & \bar{\mu}_{33} \end{bmatrix};\ C_{mms} = \begin{bmatrix} \bar{\mu}_{11} & 0 \\ 0 & \bar{\mu}_{22} \end{bmatrix}; \\ &C_{emb} = \begin{bmatrix} 0 & 0 & 0 \\ 0 & 0 & 0 \\ 0 & 0 & \bar{d}_{33} \end{bmatrix};\ C_{ems} = \begin{bmatrix} \bar{d}_{11} & 0 \\ 0 & \bar{d}_{22} \end{bmatrix} \end{aligned} \tag{15}$$

The constitutive equations for the FG-CNTRC core layer are formulated by

$$\begin{cases} \boldsymbol{\sigma}_b^c = \mathbf{C}_{uub}^c \boldsymbol{\varepsilon}_b; \\ \boldsymbol{\sigma}_s^c = \mathbf{C}_{uus}^c \boldsymbol{\varepsilon}_s \end{cases} \tag{16}$$

where

$$\boldsymbol{\sigma}_b^c = \left\{ \begin{array}{ccc} \sigma_x^c & \sigma_y^c & \tau_{xy}^c \end{array} \right\}^T; \boldsymbol{\varpi}_s^c = \left\{ \begin{array}{cc} \tau_{xz}^c & \tau_{yz}^c \end{array} \right\}^T;$$

$$\boldsymbol{C}_{uub}^c = \left[\begin{array}{ccc} Q_{11} & Q_{12} & 0 \\ Q_{12} & Q_{22} & 0 \\ 0 & 0 & Q_{66} \end{array} \right]; \mathbf{C}_{uus}^c = \left[\begin{array}{cc} Q_{44} & 0 \\ 0 & Q_{55} \end{array} \right] \tag{17}$$

$$Q_{11} = \frac{E_{11}^c}{1-\nu_{12}^c\nu_{21}^c}; Q_{22} = \frac{E_{22}^c}{1-\nu_{12}^c\nu_{21}^c}; Q_{12} = \frac{\nu_{21}^c E_{11}^c}{1-\nu_{12}^c\nu_{21}^c};$$
$$Q_{44} = G_{23}^c; Q_{55} = G_{13}^c; \; Q_{66} = G_{12}^c$$

2.4. Variational principle

Based on Hamilton's principle, the governing equation for free vibration analysis of the MEE sandwich plate with the FG-CNTRC core is described as follow

$$\int_0^t (\delta\Pi - \delta V - \delta K)\,\mathrm{d}t = 0 \tag{18}$$

where the virtual strain energy is denoted as $\delta\Pi$, the virtual work done by the external electric voltage and magnetic potential is represented as δV, while the virtual kinetic energy is symbolized by δK.

The expression for the virtual strain energy $\delta\Pi$ of the MEE sandwich plate is given by

$$\begin{aligned} \delta\Pi = & \int_{-h/2}^{-h_c/2} \left[\iint_\Omega \left\{ \begin{array}{l} \delta\text{"}_b^T \boldsymbol{\varpi}_b^f + \delta\text{"}_s^T \boldsymbol{\varpi}_s^f - \delta\mathbf{E}_b^T \mathbf{D}_b^f \\ -\delta\mathbf{E}_s^T \mathbf{D}_s^f - \delta\mathbf{H}_b^T \mathbf{B}_b^f - \delta\mathbf{H}_s^T \mathbf{B}_s^f \end{array} \right\} d\Omega \right] dz \\ & + \int_{h_c/2}^{h/2} \left[\iint_\Omega \left\{ \begin{array}{l} \delta\text{"}_b^T \boldsymbol{\varpi}_b^f + \delta\text{"}_s^T \boldsymbol{\varpi}_s^f - \delta\mathbf{E}_b^T \mathbf{D}_b^f \\ -\delta\mathbf{E}_s^T \mathbf{D}_s^f - \delta\mathbf{H}_b^T \mathbf{B}_b^f - \delta\mathbf{H}_s^T \mathbf{B}_s^f \end{array} \right\} d\Omega \right] dz \\ & + \int_{-h_c/2}^{h_c/2} \left[\iint_\Omega \left(\delta\text{"}_b^T \boldsymbol{\varpi}_b^c + \delta\text{"}_s^T \boldsymbol{\varpi}_s^c \right) d\Omega \right] dz \end{aligned} \tag{19}$$

The expression for the virtual work δV is taken by

$$\begin{aligned} & \delta V = \textstyle\int_\Omega \delta\mathbf{N}_w^T \mathbf{N}_{em} \mathbf{N}_w \mathrm{d}\Omega; \\ & \mathbf{N}_{em} = -2 \left[\begin{array}{cc} \bar{e}_{31}\varphi_0 + \bar{q}_{31}\psi_0 & 0 \\ 0 & \bar{e}_{31}\varphi_0 + \bar{q}_{31}\psi_0 \end{array} \right]; \\ & \mathbf{N}_w = \left\{ \begin{array}{c} w_{b,x} + w_{s,x} \\ w_{b,y} + w_{s,y} \end{array} \right\} \end{aligned} \tag{20}$$

The expression for the virtual kinetic energy δK is formulated as follow

$$\delta K = \int_\Omega \delta\bar{\mathbf{u}}^T \mathbf{I}_m \ddot{\bar{\mathbf{u}}} \mathrm{d}\Omega \tag{21}$$

where

$$\begin{aligned} & \bar{\mathbf{u}} = \begin{Bmatrix} \mathbf{u}_1 \\ \mathbf{u}_2 \\ \mathbf{u}_3 \end{Bmatrix}; \mathbf{u}_1 = \left\{ \begin{array}{c} u_0 \\ v_0 \\ w_b + w_s \end{array} \right\}; \mathbf{u}_2 = -\left\{ \begin{array}{c} w_{b,x} \\ w_{b,y} \\ 0 \end{array} \right\}; \\ & \mathbf{u}_3 = \left\{ \begin{array}{c} w_{s,x} \\ w_{s,y} \\ 0 \end{array} \right\}; \mathbf{I}_m = \left[\begin{array}{ccc} \mathbf{I}_0 & 0 & 0 \\ 0 & \mathbf{I}_0 & 0 \\ 0 & 0 & \mathbf{I}_0 \end{array} \right]; \mathbf{I}_0 = \left[\begin{array}{ccc} I_1 & I_2 & I_4 \\ I_2 & I_3 & I_5 \\ I_4 & I_5 & I_6 \end{array} \right]; \\ & (I_1, I_2, I_3, I_4, I_5, I_6) = \\ & \int_{-h/2}^{-h_c/2} \rho^f(z) \left(1, z, z^2, f(z), zf(z), f^2(z)\right) \mathrm{d}z \\ & + \int_{h_c/2}^{h/2} \rho^f(z) \left(1, z, z^2, f(z), zf(z), f^2(z)\right) \mathrm{d}z \\ & + \int_{-h_c/2}^{h_c/2} \rho^c(z) \left(1, z, z^2, f(z), zf(z), f^2(z)\right) \mathrm{d}z \end{aligned} \tag{22}$$

By inserting the relevant expressions into Eq. (18), the governing equation of the MEE sandwich plate is reformed by

$$\begin{aligned} & \int_\Omega \delta\bar{\boldsymbol{\varepsilon}}_b^T \bar{\mathbf{D}}_{uub} \bar{\boldsymbol{\varepsilon}}_b \mathrm{d}\Omega - \int_\Omega \delta\bar{\boldsymbol{\varepsilon}}_b^T \bar{\mathbf{D}}_{ueb} \bar{\mathbf{E}}_b \mathrm{d}\Omega \\ & - \int_\Omega \delta\bar{\boldsymbol{\varepsilon}}_b^T \bar{\mathbf{D}}_{umb} \bar{\mathbf{H}}_b \mathrm{d}\Omega + \int_\Omega \delta\boldsymbol{\gamma}_s^T \bar{\mathbf{D}}_{uus} \boldsymbol{\gamma}_s^T \mathrm{d}\Omega \\ & - \int_\Omega \delta\boldsymbol{\gamma}_s^T \bar{D}_{ues} \bar{\mathbf{E}}_s \mathrm{d}\Omega - \int_\Omega \delta\boldsymbol{\gamma}_s^T \bar{\mathbf{D}}_{ums} \bar{\mathbf{H}}_s \mathrm{d}\Omega \\ & - \int_\Omega \delta\bar{\mathbf{E}}_b^T \bar{\mathbf{D}}_{ueb}^T \bar{\boldsymbol{\varepsilon}}_b \mathrm{d}\Omega - \int_\Omega \delta\bar{\mathbf{E}}_b^T \bar{\mathbf{D}}_{eeb} \bar{\mathbf{E}}_b \mathrm{d}\Omega \\ & - \int_\Omega \delta\bar{\mathbf{E}}_b^T \bar{\mathbf{D}}_{emb} \bar{\mathbf{H}}_b \mathrm{d}\Omega - \int_\Omega \delta\bar{\mathbf{E}}_s^T \bar{\mathbf{D}}_{ues}^T \boldsymbol{\gamma}^s \mathrm{d}\Omega \\ & - \int_\Omega \delta\bar{\mathbf{E}}_s^T \bar{\mathbf{D}}_{ees} \bar{\mathbf{E}}_s \mathrm{d}\Omega - \int_\Omega \delta\bar{\mathbf{E}}_s^T \bar{\mathbf{D}}_{ems} \bar{\mathbf{H}}_s \mathrm{d}\Omega \\ & - \int_\Omega \delta\bar{\mathbf{H}}_b^T \bar{\mathbf{D}}_{umb}^T \bar{\boldsymbol{\varepsilon}}_b \mathrm{d}\Omega - \int_\Omega \delta\bar{\mathbf{H}}_b^T \bar{\mathbf{D}}_{emb} \bar{\mathbf{E}}_b \mathrm{d}\Omega \\ & - \int_\Omega \delta\bar{\mathbf{H}}_b^T \bar{\mathbf{D}}_{mmb} \bar{\mathbf{H}}_b \mathrm{d}\Omega - \int_\Omega \delta\bar{\mathbf{H}}_s^T \bar{\mathbf{D}}_{ums}^T \boldsymbol{\gamma}_s \mathrm{d}\Omega \\ & - \int_\Omega \delta\bar{\mathbf{H}}_s^T \bar{\mathbf{D}}_{ems} \bar{\mathbf{E}}_s \mathrm{d}\Omega - \int_\Omega \delta\bar{\mathbf{H}}_s^T \bar{\mathbf{D}}_{mms} \bar{\mathbf{H}}_s \mathrm{d}\Omega \\ & - \int_\Omega \delta\mathbf{N}_w^T \mathbf{N}_{em} \mathbf{N}_w \mathrm{d}\Omega - \int_\Omega \delta\bar{\mathbf{u}}^T \mathbf{I}_m \ddot{\bar{\mathbf{u}}} \mathrm{d}\Omega = 0 \end{aligned} \tag{23}$$

where

$$\bar{\boldsymbol{\varepsilon}}_b = \left\{ \begin{array}{c} \boldsymbol{\varepsilon}_{b1} \\ \boldsymbol{\varepsilon}_{b2} \\ \boldsymbol{\varepsilon}_{b3} \end{array} \right\}; \bar{\mathbf{E}}_b = -\left\{ \begin{array}{c} 0 \\ 0 \\ \varphi \end{array} \right\}; \bar{\mathbf{H}}_b = -\left\{ \begin{array}{c} 0 \\ 0 \\ \psi \end{array} \right\};$$
$$\bar{\mathbf{E}}_s = -\left\{ \begin{array}{c} \varphi_{,x} \\ \varphi_{,y} \end{array} \right\}; \bar{\mathbf{H}}_s = -\left\{ \begin{array}{c} \psi_{,x} \\ \psi_{,y} \end{array} \right\} \tag{24}$$

and

$$\bar{\mathbf{D}}_{uub} = \left[\begin{array}{ccc} \mathbf{A}^b & \mathbf{B}^b & \mathbf{E}^b \\ \mathbf{B}^b & \mathbf{D}^b & \mathbf{F}^b \\ \mathbf{E}^b & \mathbf{F}^b & \mathbf{H}^b \end{array} \right];$$
$$\left(\mathbf{A}^b, \mathbf{B}^b, \mathbf{D}^b, \mathbf{E}^b, \mathbf{F}^b, \mathbf{H}^b\right) =$$
$$\int_{-h/2}^{-h_c/2} \left(1, z, z^2, f(z), zf(z), f^2(z)\right) \mathbf{C}_{uub}^f \mathrm{d}z$$
$$+ \int_{h_c/2}^{h/2} \left(1, z, z^2, f(z), zf(z), f^2(z)\right) \mathbf{C}_{uub}^f \mathrm{d}z$$
$$+ \int_{-h_c/2}^{h_c/2} \left(1, z, z^2, f(z), zf(z), f^2(z)\right) \mathbf{C}_{uub}^c \mathrm{d}z;$$
$$\bar{\mathbf{D}}_{uus} = \int_{-h/2}^{-h_c/2} (1+f')^2 \mathbf{C}_{uus}^f \mathrm{d}z + \int_{h_c/2}^{h/2} (1+f')^2 \mathbf{C}_{uus}^f \mathrm{d}z$$
$$+ \int_{-h_c/2}^{h_c/2} (1+f')^2 \mathbf{C}_{uus}^c \mathrm{d}z;$$
$$\bar{\mathbf{D}}_{ueb} = \left\{ \begin{array}{ccc} \mathbf{C}_{ueb}^1 & \mathbf{C}_{ueb}^2 & \mathbf{C}_{ueb}^3 \end{array} \right\};$$
$$\left(\mathbf{C}_{ueb}^1, \mathbf{C}_{ueb}^2, \mathbf{C}_{ueb}^3\right) = \int_{-h/2}^{-h_c/2} \mathbf{C}_{ueb} \left(1, z, f(z)\right) g'(z) \, \mathrm{d}z$$
$$+ \int_{h_c/2}^{h/2} \mathbf{C}_{ueb} \left(1, z, f(z)\right) g'(z) \, \mathrm{d}z;$$
$$\bar{\mathbf{D}}_{umb} = \left\{ \begin{array}{ccc} \mathbf{C}_{umb}^1 & \mathbf{C}_{umb}^2 & \mathbf{C}_{umb}^3 \end{array} \right\};$$
$$\left(\mathbf{C}_{umb}^1, \mathbf{C}_{umb}^2, \mathbf{C}_{umb}^3\right) = \int_{-h/2}^{-h_c/2} \mathbf{C}_{umb} \left(1, z, f(z)\right) g'(z) \, \mathrm{d}z$$
$$+ \int_{h_c/2}^{h/2} \mathbf{C}_{umb} \left(1, z, f(z)\right) g'(z) \, \mathrm{d}z;$$
$$\bar{\mathbf{D}}_{ues} = \int_{-h/2}^{-h_c/2} \mathbf{C}_{ues} (1+f') g \mathrm{d}z + \int_{h_c/2}^{h/2} \mathbf{C}_{ues} (1+f') g \mathrm{d}z;$$
$$\bar{\mathbf{D}}_{ums} = \int_{-h/2}^{-h_c/2} \mathbf{C}_{ums} (1+f') g \mathrm{d}z + \int_{h_c/2}^{h/2} \mathbf{C}_{ums} (1+f') g \mathrm{d}z;$$
$$\bar{\mathbf{D}}_{emb} = \int_{-h/2}^{-h_c/2} \mathbf{C}_{emb} g'^2 \mathrm{d}z + \int_{h_c/2}^{h/2} \mathbf{C}_{emb} g'^2 \mathrm{d}z;$$
$$\bar{\mathbf{D}}_{ems} = \int_{-h/2}^{-h_c/2} \mathbf{C}_{ems} g^2 \mathrm{d}z + \int_{h_c/2}^{h/2} \mathbf{C}_{ems} g^2 \mathrm{d}z;$$
$$\bar{\mathbf{D}}_{eeb} = \int_{-h/2}^{-h_c/2} \mathbf{C}_{eeb} g'^2 \mathrm{d}z + \int_{h_c/2}^{h/2} \mathbf{C}_{eeb} g'^2 \mathrm{d}z;$$
$$\bar{\mathbf{D}}_{ees} = \int_{-h/2}^{-h_c/2} \mathbf{C}_{ees} g^2 \mathrm{d}z + \int_{h_c/2}^{h/2} \mathbf{C}_{ees} g^2 \mathrm{d}z;$$
$$\bar{\mathbf{D}}_{mmb} = \int_{-h/2}^{-h_c/2} \mathbf{C}_{mmb} g'^2 \mathrm{d}z + \int_{h_c/2}^{h/2} \mathbf{C}_{mmb} g'^2 \mathrm{d}z;$$
$$\bar{\mathbf{D}}_{mms} = \int_{-h/2}^{-h_c/2} \mathbf{C}_{mms} g^2 \mathrm{d}z + \int_{h_c/2}^{h/2} \mathbf{C}_{mms} g^2 \mathrm{d}z \tag{25}$$

2.5. The isogeometric approximation

Using the NURBS basic function [23], the displacement fields are approximated by following

$$\mathbf{u}^h (x, y) = \sum_{I=1}^{m \times n} \mathbf{N}_I (x, y) \, \mathbf{q}_I \tag{26}$$

in which

$$\mathbf{N}_I (x, y) = N_I (x, y) \, \mathbf{I}_{6\times 6};$$
$$\mathbf{q}_I = \left\{ \begin{array}{cccccc} u_{0I} & v_{0I} & w_{bI} & w_{sI} & \varphi_I & \psi_I \end{array} \right\}^T \tag{27}$$

where $\mathbf{I}_{6\times 6}$ is the identity matrix of size 6×6; $N_{I(x,y)}$ denotes the NURBS basic function.

Inserting Eq. (26) into Eq.(24), the bending and shear strain are rewritten as follow

$$\bar{\boldsymbol{\varepsilon}}_b = \sum_{I=1}^{m \times n} \left\{ \begin{array}{ccc} \bar{\mathbf{B}}_{b1I} & \bar{\mathbf{B}}_{b2I} & \bar{\mathbf{B}}_{b3I} \end{array} \right\}^T q_I = \sum_{I=1}^{m \times n} \bar{\mathbf{B}}_{bI} q_I;$$
$$\boldsymbol{\gamma}_s = \sum_{I=1}^{m \times n} \bar{\mathbf{B}}_{sI} q_I \tag{28}$$

in which

$$\bar{\mathbf{B}}_{b1I} = \left[\begin{array}{cccccc} N_{I,x} & 0 & 0 & 0 & 0 & 0 \\ 0 & N_{I,y} & 0 & 0 & 0 & 0 \\ N_{I,y} & N_{I,x} & 0 & 0 & 0 & 0 \end{array} \right];$$
$$\bar{\mathbf{B}}_{b2I} = -\left[\begin{array}{cccccc} 0 & 0 & N_{I,xx} & 0 & 0 & 0 \\ 0 & 0 & N_{I,yy} & 0 & 0 & 0 \\ 0 & 0 & 2N_{I,xy} & 0 & 0 & 0 \end{array} \right];$$
$$\bar{\mathbf{B}}_{b3I} = \left[\begin{array}{cccccc} 0 & 0 & 0 & N_{I,xx} & 0 & 0 \\ 0 & 0 & 0 & N_{I,yy} & 0 & 0 \\ 0 & 0 & 0 & 2N_{I,xy} & 0 & 0 \end{array} \right];$$
$$\bar{\mathbf{B}}_{sI} = \left[\begin{array}{cccccc} 0 & 0 & 0 & N_{I,x} & 0 & 0 \\ 0 & 0 & 0 & N_{I,y} & 0 & 0 \end{array} \right] \tag{29}$$

Similarly, the electric and magnetic fields are reformed as follows

$$\bar{\mathbf{E}}_b = \sum_{I=1}^{m \times n} \bar{\mathbf{B}}_{\varphi bI} \mathbf{q}_I; \bar{\mathbf{E}}_s = \sum_{I=1}^{m \times n} \bar{\mathbf{B}}_{\varphi sI} \mathbf{q}_I;$$
$$\bar{\mathbf{H}}_b = \sum_{I=1}^{m \times n} \bar{\mathbf{B}}_{\psi bI} \mathbf{q}_I; \bar{\mathbf{H}}_s = \sum_{I=1}^{m \times n} \bar{\mathbf{B}}_{\psi sI} \mathbf{q}_I \tag{30}$$

where

$$\bar{\mathbf{B}}_{\varphi bI} = \begin{bmatrix} 0 & 0 & 0 & 0 & 0 & 0 \\ 0 & 0 & 0 & 0 & 0 & 0 \\ 0 & 0 & 0 & 0 & -N_I & 0 \end{bmatrix};$$
$$\bar{\mathbf{B}}_{\varphi sI} = \begin{bmatrix} 0 & 0 & 0 & 0 & -N_{I,x} & 0 \\ 0 & 0 & 0 & 0 & -N_{I,y} & 0 \end{bmatrix};$$
$$\bar{\mathbf{B}}_{\psi bI} = \begin{bmatrix} 0 & 0 & 0 & 0 & 0 & 0 \\ 0 & 0 & 0 & 0 & 0 & 0 \\ 0 & 0 & 0 & 0 & 0 & -N_I \end{bmatrix};$$
$$\bar{\mathbf{B}}_{\psi sI} = \begin{bmatrix} 0 & 0 & 0 & 0 & 0 & -N_{I,x} \\ 0 & 0 & 0 & 0 & 0 & -N_{I,y} \end{bmatrix} \tag{31}$$

The vector $\mathbf{N}_w$ is rewritten by inserting Eq. (26) into Eq. (20), as follow

$$\mathbf{N}_w = \sum_{I=1}^{m\times n} \bar{\mathbf{B}}_{wI}\mathbf{q}_I;\ \bar{\mathbf{B}}_{wI} = \begin{bmatrix} N_{I,x} & N_{I,x} \\ N_{I,y} & N_{I,y} \end{bmatrix} \tag{32}$$

Besides substituting Eq. (26) into Eq. (22), the displacement $\bar{\mathbf{u}}$ can be rewritten as follows

$$\bar{\mathbf{u}} = \begin{Bmatrix} \mathbf{u}_1 \\ \mathbf{u}_2 \\ \mathbf{u}_3 \end{Bmatrix} = \sum_{I=1}^{m\times n} \begin{Bmatrix} \mathbf{N}_{1I} \\ \mathbf{N}_{2I} \\ \mathbf{N}_{3I} \end{Bmatrix} \mathbf{q}_I = \sum_{I=1}^{m\times n} \bar{\mathbf{N}}_I \mathbf{q}_I \tag{33}$$

in which

$$\mathbf{N}_{1I} = \begin{bmatrix} N_I & 0 & 0 & 0 & 0 & 0 \\ 0 & N_I & 0 & 0 & 0 & 0 \\ 0 & 0 & N_I & N_I & 0 & 0 \end{bmatrix};$$
$$\mathbf{N}_{2I} = \begin{bmatrix} 0 & 0 & -N_{I,x} & 0 & 0 & 0 \\ 0 & 0 & -N_{I,y} & 0 & 0 & 0 \\ 0 & 0 & 0 & 0 & 0 & 0 \end{bmatrix};$$
$$\mathbf{N}_{3I} = \begin{bmatrix} 0 & 0 & 0 & N_{I,x} & 0 & 0 \\ 0 & 0 & 0 & N_{I,y} & 0 & 0 \\ 0 & 0 & 0 & 0 & 0 & 0 \end{bmatrix} \tag{34}$$

Finally, after substituting the Eqs. (28), (30), (32) and (33) into Eq. (23), the weak form for free vibration behavior of the MEE sandwich plate with FG-CNTRC core is reformed by following

$$\left(\mathbf{K} - \omega^2\mathbf{M}\right)\bar{\mathbf{q}} = 0 \tag{35}$$

where

$$\begin{aligned}\mathbf{K} = &\int_\Omega \bar{\mathbf{B}}_b^T\bar{\mathbf{D}}_{uub}\bar{\mathbf{B}}_b\mathrm{d}\Omega - \int_\Omega \bar{\mathbf{B}}_b^T\bar{\mathbf{D}}_{ueb}\bar{\mathbf{B}}_{eb}\mathrm{d}\Omega \\ &- \int_\Omega \bar{\mathbf{B}}_b^T\bar{\mathbf{D}}_{umb}\bar{\mathbf{B}}_{mb}\mathrm{d}\Omega + \int_\Omega \bar{\mathbf{B}}_s^T\bar{\mathbf{D}}_{uus}\bar{\mathbf{B}}_s\mathrm{d}\Omega \\ &- \int_\Omega \bar{\mathbf{B}}_s^T\bar{\mathbf{D}}_{ues}\bar{\mathbf{B}}_{es}\mathrm{d}\Omega - \int_\Omega \bar{\mathbf{B}}_s^T\bar{\mathbf{D}}_{ums}\bar{\mathbf{B}}_{ms}\mathrm{d}\Omega \\ &- \int_\Omega \bar{\mathbf{B}}_{eb}^T\bar{\mathbf{D}}_{ueb}^T\bar{\mathbf{B}}_b\mathrm{d}\Omega - \int_\Omega \bar{\mathbf{B}}_{eb}^T\bar{\mathbf{D}}_{eeb}\bar{\mathbf{B}}_{eb}\mathrm{d}\Omega \\ &- \int_\Omega \bar{\mathbf{B}}_{eb}^T\bar{\mathbf{D}}_{emb}\bar{\mathbf{B}}_{mb}\mathrm{d}\Omega - \int_\Omega \bar{\mathbf{B}}_{es}^T\bar{\mathbf{D}}_{ues}^T\bar{\mathbf{B}}_s\mathrm{d}\Omega \\ &- \int_\Omega \bar{\mathbf{B}}_{es}^T\bar{\mathbf{D}}_{ees}\bar{\mathbf{B}}_{es}\mathrm{d}\Omega - \int_\Omega \bar{\mathbf{B}}_{es}^T\bar{\mathbf{D}}_{ems}\bar{\mathbf{B}}_{ms}\mathrm{d}\Omega \\ &- \int_\Omega \bar{\mathbf{B}}_{mb}^T\bar{\mathbf{D}}_{umb}^T\bar{\mathbf{B}}_b\mathrm{d}\Omega - \int_\Omega \bar{\mathbf{B}}_{mb}^T\bar{\mathbf{D}}_{emb}\bar{\mathbf{B}}_{eb}\mathrm{d}\Omega \\ &- \int_\Omega \bar{\mathbf{B}}_{mb}^T\bar{\mathbf{D}}_{mmb}\bar{\mathbf{B}}_{mb}\mathrm{d}\Omega - \int_\Omega \bar{\mathbf{B}}_{ms}^T\bar{\mathbf{D}}_{ums}^T\bar{\mathbf{B}}_s\mathrm{d}\Omega \\ &- \int_\Omega \bar{\mathbf{B}}_{ms}^T\bar{\mathbf{D}}_{ems}\bar{\mathbf{B}}_{es}\mathrm{d}\Omega - \int_\Omega \bar{\mathbf{B}}_{ms}^T\bar{\mathbf{D}}_{mms}\bar{\mathbf{B}}_{ms}\mathrm{d}\Omega;\end{aligned} \tag{36}$$
$$\mathbf{M} = \int_\Omega \bar{\mathbf{N}}^T\mathbf{I}_m\bar{\mathbf{N}}\mathrm{d}\Omega;\ \mathbf{q} = \bar{\mathbf{q}}\mathrm{e}^{i\omega t}$$

in which the stiffness matrix and mass matrix are denoted as $\mathbf{K}$ and $\mathbf{M}$, respectively; the natural frequency and mode shapes are represented as ω and $\bar{\mathbf{q}}$, respectively.

3. Numerical results

Let's consider the MEE sandwich rectangular and circular plates with different boundary conditions (BCs). The Dirichlet BCs of the rectangular plate are presented as follows

- Fully simply supported (SSSS):
  $(u_0, v_0, w_b, w_s)|_{x=0,a;y=0,b} = 0$
- Fully clamped (CCCC):
  $\begin{cases} (u_0, v_0, w_b, w_s)|_{x=0,a;y=0,b} = 0 \\ (w_{b,n}, w_{s,n})|_{x=0,a;y=0,b} = 0 \end{cases}$

In addition, the BCs of the circular are taken by

- Simply supported (SS):
  $u_0 = v_0 = w_b = w_s = 0$ at the boundary

- Clamped (CC):
  $u_0 = v_0 = w_b = w_s = w_{b,n} = w_{s,n} = 0$ at the boundary

3.1. Comparison results

In order to assess the accuracy and consistency of the present method, the free vibration of the homogeneous MEE square plate with the material properties given in Table 1 is examined. The plate is modeled by 5×5, 7×7, 9×9 and 11×11 cubic NURBS elements. The first three non-dimensional natural frequencies $\bar{\omega} = \omega R^2\sqrt{\rho/\bar{c}_{11}}$ of the SSSS homogeneous MEE square plate with various mesh sizes are presented in Table 3. The frequencies are contrasted with the ones provided by Abazid t*et al.* [39]. The comparison We can see from Table 3 that the present numerical results match very well with those given in the literature. In addition, it can be seen that the disparity between the mesh levels is inconsequential. Hence, the following analysis will involve utilizing an 11×11 element mesh. Next, the free vibration of the MEE sandwich plate with FG-CNTRC core with the material properties of the MEE face sheets and FG-CNTRC core are taken according to reference [40]. Table 4 shows the first four natural frequencies of the MEE sandwich plate with various CNTs distributions. The numerical results are compared with the findings presented in reference [40]. As we see from Table 4 , the present numerical results are in good agreement with those in the literature. The comparison results in Table 3 and Table 4 show that the current method is accurate and advantageous for the free vibration of the MEE sandwich plate with the FG-CNTRC core.

3.2. Parametric study

Firstly, the free vibration of the MEE sandwich rectangular plate with FG-CNTRC core with the material properties is given in Table 1 and Table 2 is considered in this subsection. The dimensionless natural frequency is taken by

$$\varpi = \omega a^2\sqrt{\rho_m/E_m} \tag{37}$$

Table 5 presents the influence of the initial external electric voltage φ_0, CNTs volume fraction and CNTs distribution on the first dimensionless natural frequency of the MEE sandwich square plates. While the first nondimensional natural frequency with various value of the external magnetic potential, CNTs volume fractions and CNTs distributions is tabulated in Table 6. It can be seen from Table 5 and Table 6 that an increase in the electric voltage leads to a decrease in the frequency of the MEE sandwich plate, while a rise in the magnetic potential increases the frequency. The reason is that the negative electric voltage and positive magnetic potential create compressive force, increasing the plate's stiffness. While the positive electric voltage and negative magnetic potential create the tensile force, decreasing the plate's stiffness. Besides, the dimensionless natural frequency increases as the CNTs volume fraction increases. Among the CNTs distributions, the CNT-X distribution provides the highest natural frequency, followed by CNT-UD, CNT-O and CNT-V distributions. Next, the effect of the length-to-thickness ratio on the first five dimensionless natural frequencies of the MEE sandwich plate CNT-X distribution is expressed in Table 7. We can see in Table 7 that as the length-to-thickness ratio increases, the dimensionless natural frequencies reduce. In addition, Figure 2 plots the first six mode shapes of the SSSS MEE sandwich square plate with CNT-V distribution.

Moving forward, we investigate the free vibration of the MEE sandwich circular plate with FG-CNTRC core under the simply supported (SS) and clamped (CC) boundaries. The dimensionless natural frequency is taken by. The impact of the initial electric voltage and magnetic potential on the first dimensionless natural frequency of the MEE sandwich circular plates is shown in Table 8 and Table 9, respectively. The results in Table 8 and Table 9 indicate that the negative electric voltage and positive magnetic potential enrich the stiffness of the MEE sandwich circular plates, while the positive electric voltage and negative magnetic potential reduce the natural frequency. Furthermore, the first five dimensionless natural frequencies of the MEE sandwich plate with CNT-X distribution under SS and CC boundaries with different val-

ues of the radius-to-thickness ratio are expressed in Table 10. According to Table 10, a rise in the radius-to-thickness ratio decreases the frequencies of the MEE sandwich circular plate. Finally, the first six mode shapes of the SS MEE sandwich circular plate with CNT-V distribution are plotted in Figure 3.

Tab. 3: The first three non-dimensional natural frequencies ω of the SSSS MEE square plate $a/h = 15, h_c = 0, \varphi_0 = \psi_0 = 0$.

Theory	Meshes	Mode		
		1	2	4
Ref. [39]		0.3698	0.9247	1.4568
	5x5	0.3830	0.9343	1.4588
	7x7	0.3830	0.9332	1.4573
Present	9x9	0.3830	0.9330	1.4570
	11x11	0.3830	0.9330	1.4569

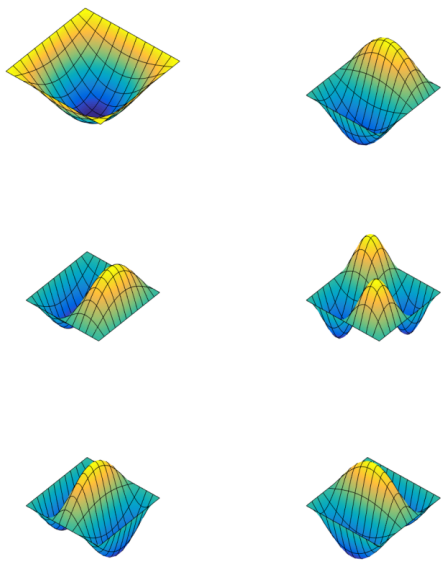

Fig. 2: The first six mode shapes of the SSSS MEE sandwich square plate with CNT-V distribution ($\hat{V}_{CNT} = 0.28, a/h = 10, h_c = 8h_f, \varphi_0 = 2V, \psi_0 = 0.2A$).

4. Conclusions

The free vibration of the MEE sandwich plates with FG-CNTRC core using the RPT and IGA is investigated in this article. The sandwich plate is composed of the homogeneous MEE face sheet and the FG-CNTRC core with various CNTs distributions and CNTs volume fractions. The current method's validity has been verified by comparing it with previous references. The impact of the CNTs distribution, CNTs volume fraction, external electric and magnetic loads and geometrical parameters on the natural frequency of the MEE sandwich plate with FG-CNTRC core is studied and discussed. The results of this article show that:

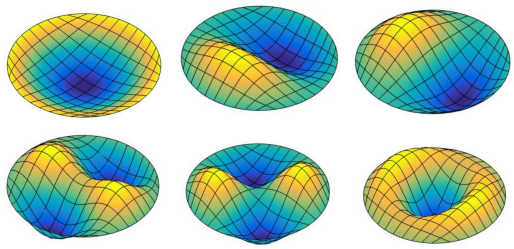

Fig. 3: The first six mode shapes of the SS MEE sandwich circular plate with CNT-V distribution ($R/h = 10, h_c = 8h_f, \varphi_0 = 2V, \psi_0 = 0.2A$).

- The stiffness of the MEE sandwich plate increases with an increase of the CNTs volume fraction.
- The CNT-X distribution provides the highest plate's stiffness, followed by CNT-UD, CNT-V and CNT-O distributions.
- The natural frequency of the MEE sandwich plate is enriched with the negative electric voltage and positive magnetic potential. With the positive electric voltage and negative magnetic potential, the frequency decreases.
- The MEE sandwich plate's stiffness is reduced by a rise of the length-to-thickness and radius-to-thickness ratios.

References

[1] Pan, E. & Han, F. (2005). Exact solution for functionally graded and layered magneto-electro-elastic plates. *Inter-*

Tab. 4: The first four natural frequencie ω of the SSSS MEE sandwich square plate with FG-CNTRC core with various CNTs distributions ($a/h = 20, h_c = 8h_f, \varphi_0 = \psi_0 = 0$).

CNTs distribution	Mode							
	1		2		3		4	
	Ref. [40]	Present	Ref. [40]	Present	Ref. [40]	Present	Ref. [40]	Present
CNT-O	1585.2	1493.3	3466.9	3428.1	3664.1	3582.7	5177.0	4924.1
CNT -V	1608.3	1534.5	3467.1	3431.5	3744.2	3685.9	5204.6	4997.6
CNT -X	1666.6	1655.3	3475.6	3513.4	3921.4	3913.1	5278.5	5201.2

Tab. 5: The effect of the initial external electric voltage φ_0 on the first dimensionless natural frequency ω of the MEE sandwich square plates with various CNTs volume fractions and CNTs distributions ($a/h = 30, h_c = 8h_f, \psi_0 = 0$).

BCs	$\hat{V}_{CNT}$	φ_0(V)	CNTs distribution			
			CNT-UD	CNT-O	CNT-V	CNT-X
SSSS	0.12	-2	0.868002	0.827914	0.847008	0.903027
		0	0.867997	0.827909	0.847004	0.903022
		2	0.867993	0.827904	0.846999	0.903018
	0.17	-2	0.916960	0.859422	0.882949	0.965232
		0	0.916955	0.859417	0.882945	0.965228
		2	0.916951	0.859412	0.882940	0.965224
	0.28	-2	0.978767	0.896432	0.923055	1.043068
		0	0.978763	0.896428	0.923051	1.043064
		2	0.978758	0.896423	0.923046	1.043061
CCCC	0.12	-2	1.434952	1.380510	1.409100	1.481397
		0	1.434948	1.380506	1.409097	1.481394
		2	1.434945	1.380503	1.409094	1.481391
	0.17	-2	1.544402	1.461811	1.500679	1.612381
		0	1.544399	1.461807	1.500676	1.612378
		2	1.544396	1.461804	1.500673	1.612375
	0.28	-2	1.643885	1.532012	1.577925	1.732468
		0	1.643882	1.532009	1.577922	1.732465
		2	1.643880	1.532006	1.577919	1.732462

national Journal of Engineering Science, *43*, 321–339.

[2] Liu, M. (2011). An exact deformation analysis for the magneto-electro-elastic fiber-reinforced thin plate. *Applied Mathematical Modelling*, *35*, 2443–246.

[3] Ramirez, F., Heyliger, P.R., & Pan, E. (2006). Free vibration response of two-dimensional magneto-electro-elastic laminated plates. *Journal of Sound and Vibration*, *292*, 626–644.

[4] Li, Y. & Zhang, J. (2013). Free vibration analysis of magnetoelectroelastic plate resting on a Pasternak foundation. *Smart materials and structures*, *23*, 025002.

[5] Ansari, R. & Gholami, R. (2017). Size-dependent buckling and postbuckling analyses of first-order shear deformable magneto-electro-thermo elastic nanoplates based on the nonlocal elasticity theory. *International Journal of Structural Stability and Dynamics*, *17*, 1750014.

[6] Malikan, M., Nguyen, V.B., & Tornabene, F. (2018). Electromagnetic forced vibrations of composite nanoplates using nonlocal strain gradient theory. *Materials Research Express*, *5*, 075031.

[7] Ebrahimi, F. & Barati, M. (2017). Buckling analysis of smart size-dependent higher order magneto-electro-thermo-elastic func-

Tab. 6: The effect of the initial external magnetic potential φ_0 on the first dimensionless natural frequency ω of the MEE sandwich square plates with various CNTs volume fractions and CNTs distributions ($a/h = 30, h_c = 8h_f, \varphi_0 = 0$).

BCs	$\hat{V}_{CNT}$	ψ_0(A)	CNTs distribution			
			CNT-UD	CNT-O	CNT-V	CNT-X
SSSS	0.12	-0.2	0.867992	0.827903	0.846998	0.903017
		0	0.867997	0.827909	0.847004	0.903022
		0.2	0.868003	0.827915	0.847009	0.903028
	0.17	-0.2	0.916950	0.859412	0.882939	0.965223
		0	0.916955	0.859417	0.882945	0.965228
		0.2	0.916960	0.896433	0.882950	0.965233
	0.28	-0.2	0.978758	0.896423	0.923046	1.043060
		0	0.978763	0.896428	0.923051	1.043064
		0.2	0.978767	0.896433	0.923056	1.043069
CCCC	0.12	-0.2	1.434945	1.380502	1.409093	1.481390
		0	1.434948	1.380506	1.409097	1.481394
		0.2	1.434952	1.380510	1.409101	1.481397
	0.17	-0.2	1.544395	1.461803	1.500673	1.612374
		0	1.544399	1.461807	1.500676	1.612378
		0.2	1.544403	1.461811	1.500680	1.612381
	0.28	-0.2	1.643879	1.532006	1.577918	1.732462
		0	1.643882	1.532009	1.577922	1.732465
		0.2	1.643886	1.532013	1.577925	1.732468

Tab. 7: The first five dimensionless natural frequencies ω of the MEE sandwich square plate with CNT-X distribution with various length-to-thickness ratios ($\hat{V}_{CNT} = 0.17, h_c = 8h_f, \varphi_0 = 2V, \psi_0 = 0.2A$).

BCs	Mode	a/h				
		10	20	30	40	50
SSSS	1	2.108332	1.355757	0.965229	0.742497	0.601290
	2	3.922911	2.752328	2.030846	1.587484	1.296244
	3	3.980277	3.102333	2.429263	1.958130	1.626248
	4	5.323155	4.216746	3.340833	2.711599	2.261280
	5	6.029627	4.712948	3.647055	2.920779	2.416879
CCCC	1	2.699028	2.074631	1.612378	1.294057	1.071966
	2	4.473461	3.548905	2.791298	2.254934	1.874969
	3	4.517688	3.762351	3.159931	2.665353	2.277303
	4	5.851219	4.923942	4.127224	3.475281	2.965827
	5	6.529568	5.453332	4.450759	3.677937	3.101044

tionally graded nanosize beams. *Journal of Mechanics*, *33*, 23–33.

[8] Xin, L. & Hu, Z. (2015). Free vibration of simply supported and multilayered magneto-electro-elastic plates. *Composite structures*, *121*, 344–350.

[9] Razavi, S. (2017). On the Buckling the Behavior of a Multiphase Smart Plate based on a Higher-order Theory. *Mechanics of Advanced Composite Structures*, *4*, 47–58.

[10] Shooshtari, A. & Razavi, S. (2016). Vibration analysis of a magnetoelectroelastic rectangular plate based on a higher-order shear deformation theory. *Latin American Journal of Solids and Structures*, *13*, 554–572.

Tab. 8: The effect of the initial external electric voltage φ_0 on the first dimensionless natural frequency ω' of the MEE sandwich circular plates with various CNTs volume fractions and CNTs distributions($R/h = 30, h_c = 8h_f, \psi_0 = 0$).

BCs	$\hat{V}_{CNT}$	$\varphi_0(V)$	CNTs distribution			
			CNT-UD	CNT-O	CNT-V	CNT-X
SS	0.12	-2	0.241137	0.225318	0.233671	0.254942
		0	0.241132	0.225312	0.233666	0.254938
		2	0.241127	0.225307	0.233661	0.254933
	0.17	-2	0.255442	0.233602	0.243743	0.273711
		0	0.255438	0.233597	0.243738	0.273706
		2	0.255433	0.233592	0.243733	0.273702
	0.28	-2	0.277734	0.246482	0.258505	0.301990
		0	0.277730	0.246477	0.258500	0.301986
		2	0.277725	0.246472	0.258495	0.301982
CC	0.12	-2	0.457264	0.433853	0.446235	0.478033
		0	0.457260	0.433850	0.446232	0.478030
		2	0.457257	0.433847	0.446229	0.478027
	0.17	-2	0.484405	0.450911	0.466961	0.513159
		0	0.484402	0.450908	0.466958	0.513156
		2	0.484399	0.450905	0.466955	0.513153
	0.28	-2	0.520791	0.472470	0.493125	0.560107
		0	0.520788	0.472467	0.493122	0.560104
		2	0.520785	0.472465	0.493119	0.560102

[11] Yang, Y. & Li, X.F. (2019). Bending and free vibration of a circular magnetoelectroelastic plate with surface effects. *International Journal of Mechanical Science*, *157*, 858–871.

[12] Sobhy, M. & Mukahal, F.A. (2022). Analysis of electromagnetic effects on vibration of functionally graded GPLs reinforced piezoelectromagnetic plates on an elastic substrate. *Crystals*, *12*, 487.

[13] Arefi, M. & Amabili, M. (2021). A comprehensive electro-magneto-elastic buckling and bending analyses of three-layered doubly curved nanoshell, based on nonlocal three-dimensional theory. *Composite Structures*, *257*, 113100.

[14] Mohammadrezazadeh, S. (2023). Vibration of MEE Composite Conical Shell Surrounded by Nonlinear Elastic Foundation Considering the Effect of Geometrical Nonlinearity. *Mechanics Of Advanced Composite Structures*, *10*, 85–102.

[15] Shen, H.S. (2009). Nonlinear bending of functionally graded carbon nanotube-reinforced composite plates in thermal environments. *Composite Structures*, *91*, 9–19.

[16] Wang, Z.X. & Shen, H.S. (2011). Nonlinear vibration of nanotube-reinforced composite plates in thermal environments. *Computational Materials Science*, *50*, 2319–2330.

[17] Lei, Z., Zhang, L., & Liew, K. (2015). Free vibration analysis of laminated FG-CNT reinforced composite rectangular plates using the kp-Ritz method. *Composite Structures*, *127*, 245–259.

[18] Zhang, L., Lei, Z., & Liew, K. (2015). Vibration characteristic of moderately thick functionally graded carbon nanotube reinforced composite skew plates. *Composite Structures*, *122*, 172–183.

[19] Pouresmaeeli, S. & Fazelzadeh, S. (2016). Frequency analysis of doubly curved functionally graded carbon nanotube-reinforced

Tab. 9: The effect of the initial external magnetic potential ψ_0 on the first dimensionless natural frequency ω' of the MEE sandwich circular plates with various CNTs volume fractions and CNTs distributions ($R/h = 30, h_c = 8h_f, \varphi_0 = 0$).

BCs	$\hat{V}_{CNT}$	$\psi_0(A)$	CNTs distribution			
			CNT-UD	CNT-O	CNT-V	CNT-X
SS	0.12	-0.2	0.241126	0.225306	0.233660	0.254932
		0	0.241132	0.225312	0.233666	0.254938
		0.2	0.241138	0.225319	0.233672	0.254943
	0.17	-0.2	0.255432	0.233591	0.243732	0.273701
		0	0.255438	0.233597	0.243738	0.273706
		0.2	0.255443	0.233603	0.243744	0.273712
	0.28	-0.2	0.277724	0.246471	0.258495	0.301981
		0	0.277730	0.246477	0.258500	0.301986
		0.2	0.277735	0.246483	0.258506	0.301991
CC	0.12	-0.2	0.457257	0.433846	0.446228	0.478026
		0	0.457260	0.433850	0.446232	0.478030
		0.2	0.457264	0.433854	0.446236	0.478033
	0.17	-0.2	0.484398	0.450904	0.466954	0.513153
		0	0.484402	0.450908	0.466958	0.513156
		0.2	0.484405	0.450912	0.466961	0.513159
	0.28	-0.2	0.520785	0.472464	0.493118	0.560101
		0	0.520788	0.472467	0.493122	0.560104
		0.2	0.520791	0.472471	0.493125	0.560107

Tab. 10: The first five dimensionless natural frequencies ω' of the MEE sandwich circular plate with CNT-X distribution with various radius-to-thickness ratios ($\hat{V}_{CNT} = 0.28, h_c = 8h_f, \varphi_0 = 2V, \psi_0 = 0.2A$).

BCs	Mode	a/h				
		10	20	30	40	50
SS	1	0.794141	0.442607	0.301987	0.228399	0.183440
	2	1.626570	0.964021	0.668588	0.508848	0.409916
	3	1.843419	1.219506	0.877237	0.677783	0.550098
	4	2.613720	1.678500	1.192295	0.916200	0.741559
	5	2.690386	1.844647	1.346837	1.047567	0.853134
CC	1	1.206416	0.783829	0.560105	0.431504	0.349699
	2	2.061505	1.365183	0.982391	0.759117	0.616138
	3	2.170988	1.610716	1.223259	0.969566	0.797539
	4	2.999691	2.105085	1.549751	1.210093	0.987516
	5	3.025821	2.264112	1.728297	1.373547	1.131525

composite panels. *Acta Mechanica*, *227*, 2765–2794.

[20] Ansari, R., Torabi, J., & Hassani, R. (2019). Vibration analysis of FG-CNTRC plates with an arbitrarily shaped cutout based on the variational differential quadrature finite element method. *Materials Research Express*, *6*, 125086.

[21] Dat, N.D., Thanh, N.V., Minh-Anh, V., & Duc, N.D. (2022). Vibration and nonlinear dynamic analysis of sandwich FG-CNTRC plate with porous core layer. *Mechanics of Advanced Materials and Structures*, *29*, 1431–1448.

[22] Cheshmeh, E., Karbon, M., Eyvazian, A., Jung, D.W., Habibi, M., , & Safarpour,

M. (2022). Buckling and vibration analysis of FG-CNTRC plate subjected to thermo-mechanical load based on higher order shear deformation theory. *Mechanics Based Design of Structures and Machines*, *50*, 1137–1160.

[23] Hughes, T.J., Cottrell, J.A., & Bazilevs, Y. (2005). Isogeometric analysis: CAD, finite elements, NURBS, exact geometry and mesh refinement. *Computer methods in applied mechanics and engineering*, *194*, v.

[24] Bazilevs, Y., Takizawa, K., Tezduyar, T.E., Hsu, M.C., Otoguro, Y., & Mochizuki, H. (2020). Wind Turbine and Turbomachinery Computational Analysis with the ALE and Space-Time Variational Multiscale Methods and Isogeometric Discretization. *Journal of Advanced Engineering and Computation*, *4*, 1–32.

[25] Takizawa, K., Bazilevs, Y., Tezduyar, T.E., Hsu, M.C., & Terahara, T. (2022). Computational Cardiovascular Medicine With Isogeometric Analysis. *Journal of Advanced Engineering and Computation*, *6*, 1–32.

[26] Zhang, Y., Ren, H., , & Rabczuk, T. (2022). Nonlocal Operator Method for Solving Partial Differential Equations: State-of-the-Art Review and Future Perspectives. *Journal of Advanced Engineering and Computation*, *6*, 1–35.

[27] Thai, C.H., Ferreira, A., & Nguyen-Xuan, H. (2018). Isogeometric analysis of size-dependent isotropic and sandwich functionally graded microplates based on modified strain gradient elasticity theory. *Composite Structures*, *192*, 274–288.

[28] Thai, C.H., Ferreira, A., & Phung-Van, P. (2019). Size dependent free vibration analysis of multilayer functionally graded GPLRC microplates based on modified strain gradient theory. *Composites Part B: Engineering*, *169*, 174–188.

[29] Thai, C.H., Ferreira, A., Rabczuk, T., & Nguyen-Xuan, H. (2018). Size-dependent analysis of FG-CNTRC microplates based on modified strain gradient elasticity theory. *European Journal of Mechanics-A/Solids*, *72*, 521–538.

[30] Gholami, R., Ansari, R., & Gholami, Y. (2017). Size-dependent bending, buckling and vibration of higher-order shear deformable magneto-electro-thermo-elastic rectangular nanoplates. *Materials Research Express*, *4*, v.

[31] Mohammadimehr, M., Okhravi, S., & Alavi, S.A. (2018). Free vibration analysis of magneto-electro-elastic cylindrical composite panel reinforced by various distributions of CNTs with considering open and closed circuits boundary conditions based on FSDT. *Journal of Vibration and Control*, *24*, 1551–1569.

[32] Shen, H.S. & Wang, H. (2017). Nonlinear vibration of compressed and thermally postbuckled nanotube-reinforced composite plates resting on elastic foundations. *Aerospace Science and Technology*, *64*, 63–74.

[33] Sofiyev, A., Turkaslan, B.E., Bayramov, R., & Salamci, M. (2019). Analytical solution of stability of FG-CNTRC conical shells under external pressures. *Thin-Walled Structures*, *144*, 106338.

[34] Senthilnathan, N., Lim, S., Lee, K., & Chow, S. (1987). Buckling of shear-deformable plates. *AIAA journal, vol*, *25*, 1268–1271.

[35] Yin, S., Hale, J.S., Yu, T., Bui, T.Q., & Bordas, S.P. (2014). Isogeometric locking-free plate element: a simple first order shear deformation theory for functionally graded plates. *Composite Structures*, *118*, 121–138.

[36] Ke, L.L., Wang, Y.S., Yang, J., & Kitipornchai, S. (2014). Free vibration of size-dependent magneto-electro-elastic nanoplates based on the nonlocal theory. *Acta Mechanica Sinica*, *30*, 516–525.

[37] Jamalpoor, A., Ahmadi-Savadkoohi, A., Hosseini, M., & Hosseini-Hashemi, S. (2017). Free vibration and biaxial buckling analysis of double magneto-electro-elastic nanoplate-systems coupled by a

visco- Pasternak medium via nonlocal elasticity theory. *European Journal of Mechanics - A/Solids*, *63*, 84–98.

[38] Malikan, M. & Nguyen, V.B. (2018). Buckling analysis of piezo-magnetoelectric nanoplates in hygrothermal environment based on a novel one variable plate theory combining with higher-order nonlocal strain gradient theory. *Physica E: Low-dimensional Systems and Nanostructures*, *102*, 8–28.

[39] Abazid, M.A. (2019). The nonlocal strain gradient theory for hygrothermo-electromagnetic effects on buckling, vibration and wave propagation in piezo-electromagnetic nanoplates. *International Journal of Applied Mechanics*, *11*, 1950067.

[40] Dat, N.D., Quan, T.Q., Mahesh, V., & Duc, N.D. (2020). Analytical solutions for nonlinear magneto-electro-elastic vibration of smart sandwich plate with carbon nanotube reinforced nanocomposite core in hygrothermal environment. *International Journal of Mechanical Sciences*, *186*, 105906.

About Authors

Hung Tan PHAM was born in Vietnam in 1981. He has a Ph.D. degree in Mechanics. Now, he is a lecturer at the Faculty of Civil Engineering at Ho Chi Minh City University of Technology and Education, Ho Chi Minh City, Vietnam. His research interests are the computational mechanics.

Trung Thanh NGUYEN was born in Vietnam in 1987. He has a M.EnG in Civil Engineering. Now, he is working at the Faculty of Civil Engineering at Ho Chi Minh City University of Technology (HUTECH University), Ho Chi Minh City, Vietnam.

Huy Gia NGUYEN was born in Vietnam in 1993. He has a M.EnG in Civil Engineering. Now, he is working at Ho Chi Minh City University of Technology (HUTECH University), Ho Chi Minh City, Vietnam.

Phuc Van PHUNG received his Ph.D from Ghent University in 2016. He has been conducting computational mechanics research since 2012. Currently, he is a senior lecturer at the Faculty of Civil Engineering, HUTECH University, Ho Chi Minh City, Vietnam. He has published over 58 Web-of-Science-indexed journal articles on computational and structural mechanics and nanostructures. He is one of World's Best Mechanical and Aerospace Engineering Scientists according to Research.com. He is also one of Best Rising Stars of Science in the World - 2022.